Nano-Micro Letters

ISSN 2311-6706
e-ISSN 2150-5551
CN 31-2103/TB

ARTICLE

https://doi.org/10.1007/s40820-020-00475-5



**Cite as**
Nano-Micro Lett.
(2020) 12:139

Received: 7 April 2020
Accepted: 2 June 2020
Published online: 1 July 2020


# Strongly Anchoring Polysulfides by Hierarchical $Fe_3O_4/C_3N_4$ Nanostructures for Advanced Lithium–Sulfur Batteries

Soochan Kim[1], Simindokht Shirvani-Arani[2], Sungsik Choi[1], Misuk Cho[1], Youngkwan Lee[1] ✉

✉ Youngkwan Lee, yklee@skku.edu

[1] School of Chemical Engineering, Sungkyunkwan University, Suwon 16419, Republic of Korea

[2] Nuclear Science and Technology Research Institute (NSTRI), Tehran 14395-834, Iran

## HIGHLIGHTS

- A multi-functional interlayer for Li–S batteries has been developed to efficiently regulate the shuttle effect and enhance the sulfur utilization using hierarchical $Fe_3O_4/C_3N_4$ nanostructures.
- $C_3N_4$ nanotube exhibits high surface area and high affinity toward LPS, and the decorating $Fe_3O_4$ nanospheres on the surface of $C_3N_4$ nanotube accelerate the adsorption of LPS and improve the electronic pathways.
- The combination of $Fe_3O_4$ nanospheres and $C_3N_4$ nanotube leads to remarkable battery performance with 400% improvements in specific capacity compared with Li–S battery without using interlayer and a low capacity decay per cycle of 0.02% at 2 C over 1000 cycles.

**ABSTRACT** Li–S batteries have attracted considerable interest as next-generation energy storage devices owing to high energy density and the natural abundance of sulfur. However, the practical applications of Li–S batteries are hampered by the shuttle effect of soluble lithium polysulfides (LPS), which results in low cycle stability. Herein, a functional interlayer has been developed to efficiently regulate the LPS and enhance the sulfur utilization using hierarchical nanostructure of $C_3N_4$ ($t$-$C_3N_4$) embedded with $Fe_3O_4$ nanospheres. $t$-$C_3N_4$ exhibits high surface area and strong anchoring of LPS, and the $Fe_3O_4$/$t$-$C_3N_4$ accelerates the anchoring of LPS and improves the electronic pathways. The combination of these materials leads to remarkable battery performance with 400% improvement in a specific capacity and a low capacity decay per cycle of 0.02% at 2 C over 1000 cycles, and stable cycling at 6.4 mg $cm^{-2}$ for high-sulfur-loading cathode.

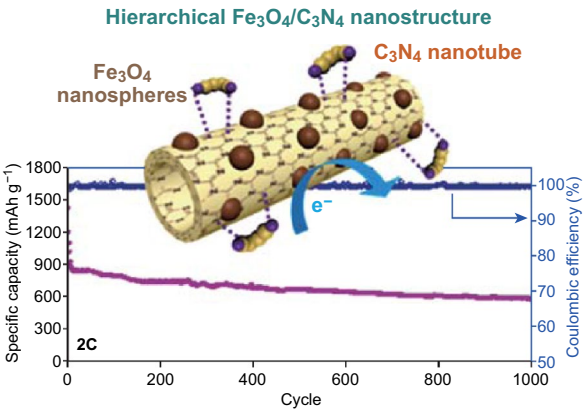


**KEYWORDS** Hierarchical nanostructured $C_3N_4$; $Fe_3O_4$ nanosphere; Interlayer; Long-term cycling; Lithium–sulfur battery

## 1 Introduction

Rechargeable lithium–sulfur batteries (LSBs) are widely expected to be the next-generation high-density energy storage technology due to their high theoretical capacity and high energy density, as well as the natural abundance and environmental compatibility of sulfur [1, 2]. However, the practical applications of LSBs are still hampered by intrinsic issues, such as the large volumetric expansion (80%) of sulfur upon lithiation, insulating properties of sulfur, and dissolution of intermediate lithium polysulfides (LPS) species during cycling [1–3]. Shuttle effects, which are a result of the elution of LPS, are considered to be the main issue, resulting in the low Coulombic efficiency, high self-discharge, poor rate performance, and low charge–discharge cycles of LSBs [3, 4]. To address this main issue, several strategies to regulate the LPS have been explored by various research groups. The most studies are focused on the control of the LPS generated from the sulfur cathode, such as the encapsulation of sulfur and the development of functional polymer binders for LSB. These approaches have led to the improved suppression of the LPS shuttle effect, but they do not control the LPS generated after long-term cycling and the resulting LPS passivate the Li-metal surface [5, 6].

Recently, an interlayer has been introduced for the effective adsorption of LPS and for the reuse of the adsorbed active material on the outside of the cathode. Various carbon materials have been used as interlayers. To improve their LPS adsorption properties, N, O, or S doping, combination with various carbon materials, and composites with metal compounds are introduced [7–11].

In particular, N-doped carbon materials effectively inhibit the LPS shuttle effect and lead to prolonged battery cycling due to the strong chemical interactions formed between the electronegative nitrogen atoms and the Li ions in the LPS [12–14]. However, the introduction of N-doped graphene and N-doped carbon nanotubes complicates the manufacturing process and is expensive [15, 16]. In contrast, graphitic carbon nitride (g-$C_3N_4$), which contains tri-s-triazine units connected to planar amino groups in each layer, is a promising functional material owing to its inexpensive precursor, easy manufacturing process, and high nitrogen content (> 60%) [16, 17]. However, the limited surface area and relatively low electrical conductivity of g-$C_3N_4$ are significant challenges to be solved because they can cause inadequate battery performance.

In this work, we have introduced a hierarchical nanostructured $C_3N_4$-based material for use as an interlayer with improved electrical conductivity and efficient anchoring LPS. For the hierarchical nanostructures, tubular $C_3N_4$ (*t*-$C_3N_4$) is prepared from cheap melamine without template and $Fe_3O_4$ nanospheres are decorated on the surface of *t*-$C_3N_4$ by facile synthetic method. Tubular morphology of $C_3N_4$ exhibits a high surface area, which results in an increase in its contact with the LPS. $Fe_3O_4$ nanoparticles are known as having high interaction with LPS, excellent electrical conductivity, and low cost among various metal oxides [18]. The as-developed hierarchical tubular $C_3N_4$ (*t*-$C_3N_4$) embedded with $Fe_3O_4$ nanospheres ($Fe_3O_4$/*t*-$C_3N_4$) has been applied as an interlayer and shows remarkable battery performance with 400% improvements in specific capacity compared with LSB without using interlayer and a low capacity decay per cycle of 0.02% at 2 C over 1000 cycles. Moreover, it presented the stable cycling at 6.4 mg $cm^{-2}$ for high-sulfur-loading cathode. With facile synthesis, low-cost precursors, and low toxic materials, optimally designed $Fe_3O_4$/*t*-$C_3N_4$ for sulfur cathode would be a new approach for high-performance energy storage devices.

## 2 Experimental

### 2.1 Materials

Melamine, $FeSO_4 \cdot 7H_2O$, $FeCl_3 \cdot 6H_2O$, NaOH, sulfur, lithium metal, bis(trifluoromethyl sulfonyl)amine lithium salt (LiTFSI), 1,3-dioxolane (DOL), dimethoxyethane (DME), and poly(vinylidene fluoride) (PVdF) ($M_w$ 530,000 g $mol^{-1}$) were purchased from Sigma-Aldrich (USA). Lithium nitrate ($LiNO_3$), $Li_2S$, and *N*-methyl-2-pyrrolidinone (NMP) were purchased from Alfa Aesar (USA).

### 2.2 Synthesis of g-$C_3N_4$ and t-$C_3N_4$

g-$C_3N_4$ was prepared via thermal polymerization using melamine as a precursor. Melamine powder (3 g) was heated in air to 550 °C at a heating rate of 10 °C $min^{-1}$. The g-$C_3N_4$ product was obtained after being heated at 550 °C for 5 h and naturally cooled to room temperature. *t*-$C_3N_4$ was obtained via a two-step process based on rolling-up


https://doi.org/10.1007/s40820-020-00475-5

mechanism (detailed in electronic supplementary material). Firstly, melamine (3 g) was added to 30 mL of deionized water and dispersed for 30 min using tip sonication (750 W, VCX 750, Sonics, USA). The resulting mixture was heated in a Teflon-lined autoclave at 200 °C for 12 h. After the autoclave was cooled to room temperature, a white powder was obtained. Following filtration and washing with deionized water and ethanol for three times, the white powder was ground in an agate mortar for 30 min. The ground white powder was heated under above-mentioned conditions to give the *t*-$C_3N_4$ product (heated in air to 550 °C at a heating rate of 10 °C $min^{-1}$ and 550 °C for 5 h).

### 2.3 Synthesis of Hierarchical Nanostructured $C_3N_4$ Embedded with $Fe_3O_4$ Nanospheres ($Fe_3O_4$/t-$C_3N_4$)

A specific amount of *t*-$C_3N_4$ was dispersed in ethanol/$H_2O$ (1:1) using ultrasonication for 2 h. An aqueous solution containing $FeSO_4 \cdot 7H_2O$ (1.313 mmol) and $FeCl_3 \cdot 6H_2O$ (1.85 mmol) was prepared and specific aliquots of the resulting solution were then added to the *t*-$C_3N_4$-containing suspension under vigorous stirring at 80 °C. After 10 min, 2 M NaOH solution was rapidly added to the above-mentioned solution to reach a pH of ~ 10. After stirring for 30 min at 80 °C, the resulting black mixture was allowed to cool to room temperature. The mixture was washed several times with $H_2O$ and ethanol and then dried in an oven at 60 °C for 12 h to obtain the $Fe_3O_4$-decorated *t*-$C_3N_4$ product. According to the amount of *t*-$C_3N_4$ used, L-$Fe_3O_4$/*t*-$C_3N_4$ (low concentration of $Fe_3O_4$), $Fe_3O_4$/*t*-$C_3N_4$, and H-$Fe_3O_4$/*t*-$C_3N_4$ (high concentration of $Fe_3O_4$) were obtained.

### 2.4 Preparation of Interlayer

The interlayer was obtained by coating the as-synthesized material on a Celgard (2500) membrane. g-$C_3N_4$, *t*-$C_3N_4$ or $Fe_3O_4$/*t*-$C_3N_4$, carbon black (CB), and 5 wt % PVdF (in NMP) were mixed in a weight ratio of 6/3/1 (as-synthesized materials/CB/binder, *w*/*w*/*w*) using high-energy ball milling (8000D, SPEX, USA). The mixed slurry was then homogeneously coated onto the Celgard (2500) membrane using a doctor blade. The interlayer was dried at 50 °C under an air atmosphere for 12 h and at 60 °C in vacuum for 3 h. The typical loading was 0.3–0.5 g $cm^{-2}$.

### 2.5 Characterization

The morphology and EDS analysis of the as-prepared materials (g-$C_3N_4$, *t*-$C_3N_4$, and $Fe_3O_4$/*t*-$C_3N_4$) were obtained using transmission electron microscopy (TEM, JEM-2010, JEOL, Japan). The surface morphology of the interlayer was observed using scanning electron microscopy (SEM, JSM-6390A and JSM-7500F, JEOL, Japan). X-ray diffraction (XRD) patterns were collected using a D8 Advance diffractometer (Bruker, Germany) equipped with a Cu Kα radiation source (λ = 1.54056 Å). X-ray photoelectron spectroscopy (XPS) was performed using an ESCA 2000 spectrometer (VG Scientific, USA) with an Al-Kα X-ray source operated at 170 W (13 mA and 13 kV). Raman spectra were obtained to characterize $Fe_3O_4$/*t*-$C_3N_4$ at room temperature (RT) using Raman spectrometry (DXR2xi, Thermo Fisher, USA) with a 785-nm laser excitation source. Elemental analysis (EA) was conducted using a Vario EL cube (Elementar, Germany). Thermogravimetric analysis (TGA) was performed from 25 to 800 °C at a heating rate of 10 °C $min^{-1}$ under a flow of $N_2$ using a Seiko Exstar 6000 TG/DTA6100 instrument (Seiko, Japan). The specific surface area (BET) was determined on a surface area analyzer (ASAP 2020 Plus, Micromeritics Instruments, USA) using the Brunauer–Emmett–Teller method. Electrical impedance spectroscopy (EIS) was performed on a potentiostat (VSP, BioLogic, France). The LPS adsorption capability was evaluated using UV–Vis spectroscopy (8453 UV–visible Spectroscopy System, Agilent, USA) and the LPS adsorption capability of prepared interlayer was observed using H-type cells.

### 2.6 Electrochemical Characterization

Electrochemical characterization was carried out using CR2032-type coin cells. To prepare the sulfur cathode, the sulfur/CB composite (7/3, *w*/*w*), CB, and 5 wt% PVdF (in NMP) were mixed in a weight ratio of 8:1:1 (sulfur composites/CB/binder, *w*/*w*/*w*) using high-energy ball

milling. The mixed slurry was then homogeneously coated onto aluminum foil (20 μm, thickness) via a doctor blade. Finally, the electrodes were dried at 50 °C under an air atmosphere for 12 h and at 50 °C in vacuum for 6 h. The typical sulfur loading was 0.8–1.0 mg $cm^{-2}$. In the case of a high-sulfur loading, the cathodes were fabricated on carbon paper (AvCarb, Ballard, USA) using a similar procedure to that described above. The electrolyte was a mixture of DOL and DME (1:1, *v/v*) containing 1 M LiTFSI and 0.2 M $LiNO_3$ and added to Li–S cell with a ratio of 20 μL/mg-S. The Li–S cells were assembled in a 2032-type coin cell using the sulfur cathode as the working electrode, lithium metal as the counter electrode, and the Celgard membrane (2500) or fabricated interlayer as the separator in an Ar-filled glove box containing < 10 ppm $H_2O$ and $O_2$. The galvanostatic discharge–charge behavior was monitored using a battery test system (WonATech Corp., Republic of Korea) over a voltage range of 1.7–2.8 V vs. $Li/Li^+$ at 25 °C and all the Li–S cells were activated at 0.05 C for two cycles prior to measurement. EIS measurements were conducted using a potentiostat (VSP, BioLogic, France) upon applying a 50-mV-amplitude sine wave in the frequency range of 0.1 Hz to 100 kHz.

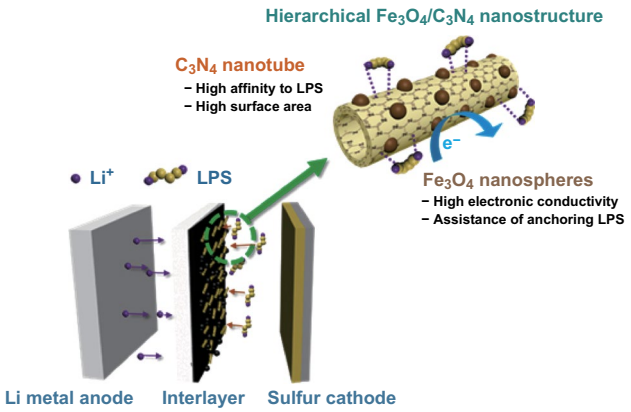


**Fig. 1** A schematic representation of the roles of the $Fe_3O_4/t\text{-}C_3N_4$ interlayer

## 3 Results and Discussion

### 3.1 Characterization of $Fe_3O_4/t\text{-}C_3N_4$

Figure 1 illustrates the roles of the $Fe_3O_4/t\text{-}C_3N_4$ interlayer in the effective anchoring LPS, preventing dissolved LPS from traveling to the lithium metal anode during the discharge process. $t\text{-}C_3N_4$ exhibits a high affinity for LPS and high surface area, and the decorated $Fe_3O_4$ nanospheres on $t\text{-}C_3N_4$ provide high electronic conductivity and contribute additional LPS adsorption and sulfur utilization.

XRD, XPS, TGA, and TEM were used to confirm the structure of the as-prepared materials (g-$C_3N_4$, $t\text{-}C_3N_4$, and

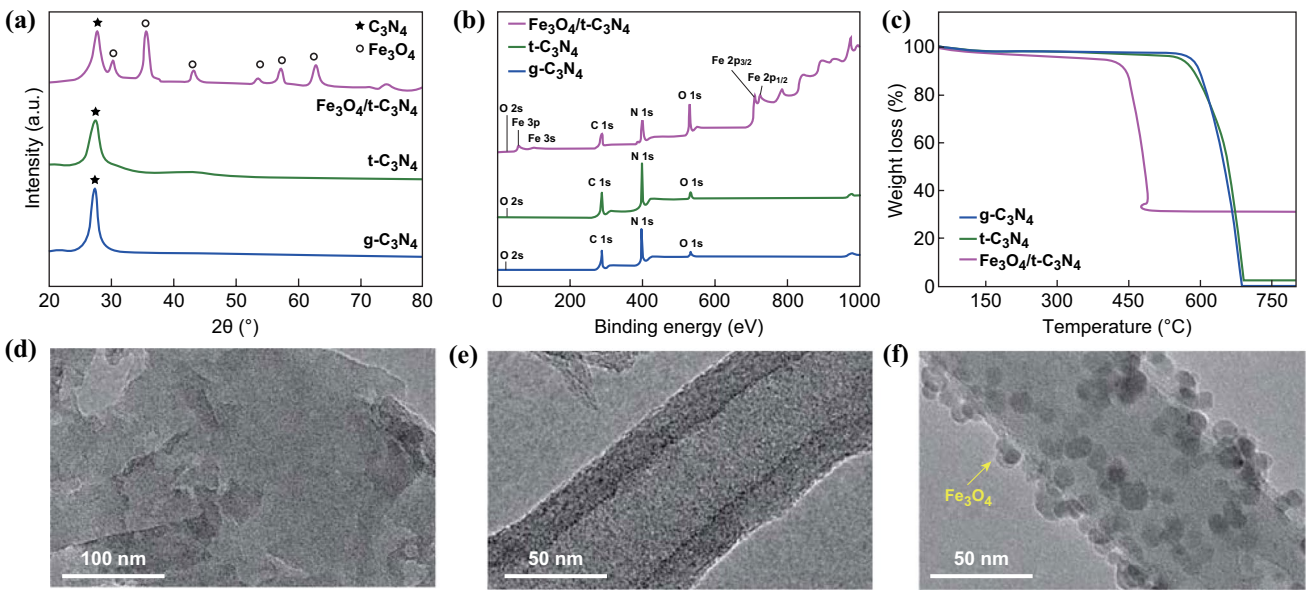


**Fig. 2** **a** XRD patterns, **b** XPS spectra, and **c** TGA curves obtained for g-$C_3N_4$, $t\text{-}C_3N_4$, and $Fe_3O_4/t\text{-}C_3N_4$. TEM images recorded for **d** g-$C_3N_4$, **e** $t\text{-}C_3N_4$, and **f** $Fe_3O_4/t\text{-}C_3N_4$


https://doi.org/10.1007/s40820-020-00475-5

$Fe_3O_4$/*t*-$C_3N_4$), as shown in Fig. 2. All of the as-prepared materials exhibit a specific peak corresponding to g-$C_3N_4$, which suggests that the samples have the same basic crystal structure of g-$C_3N_4$ (JCPDS No. 87-1526). The strong interplanar stacking peak of g-$C_3N_4$ observed at 27.2° (002), which corresponds to the aromatic systems, was shifted to 27.5° in *t*-$C_3N_4$, indicating the decreased gallery distance between the basic sheets of *t*-$C_3N_4$ [19, 20]. In the case of $Fe_3O_4$/*t*-$C_3N_4$, the low-angle reflection peak was shifted to 27.7°, which was mainly attributed to the simultaneous decrease in the planar size of the layers and the formation of $Fe_3O_4$ nanospheres. Considering the characteristic peaks of $Fe_3O_4$ (JCPDS No. 19-0629), the presence of $Fe_3O_4$ nanospheres on *t*-$C_3N_4$ does not influence the crystal structure of *t*-$C_3N_4$, which is advantageous for its affinity toward LPS and enhancement of electronic conductivity by sharing their respective effects.

XPS was employed to investigate the valence states and chemical environment of the constituent elements on the surface of the g-$C_3N_4$, *t*-$C_3N_4$, and $Fe_3O_4$/*t*-$C_3N_4$ materials (Figs. 2b and S1). Both g-$C_3N_4$ and *t*-$C_3N_4$ display similar N 1 s spectra, which confirm the existence of a graphite-like $sp^2$-bonded structure. Moreover, two peaks were observed at 725 and 711 eV in the Fe 2p spectrum recorded for the $Fe_3O_4$/*t*-$C_3N_4$, which were assigned to Fe $2p_{1/2}$ and Fe $2p_{3/2}$, respectively (Fig. S1a). Detailed N 1 s peaks are shown in Fig. S1b. The values are almost equal to the standard binding energy of $Fe_3O_4$, suggesting $Fe_3O_4$ deposited on the region of *t*-$C_3N_4$ [21, 22]. Moreover, the $Fe_3O_4$/*t*-$C_3N_4$ is characterized by Raman spectroscopy (detailed in Fig. S2).

To confirm the thermal properties of the as-prepared materials, TGA was performed under a flow of $N_2$ from 25 to 800 °C (Fig. 2c). g-$C_3N_4$ and *t*-$C_3N_4$ are stable below 550 °C. When the temperature increases above 550 °C, the decomposition of $C_3N_4$ occurs and is completed at 700 °C. For $Fe_3O_4$/*t*-$C_3N_4$, the TGA curve was shifted to lower temperature due to the catalytic effects of $Fe_3O_4$ nanospheres on the oxidation of *t*-$C_3N_4$ [23]. Using the residual weight observed at > 440 °C, the $Fe_3O_4$ content was determined to be ~ 30 wt%. Moreover, through elemental analysis (EA, CHN mode), composition of g-$C_3N_4$ and *t*-$C_3N_4$ was further confirmed (Table S2). In the present investigation, the theoretical value of C/N atomic ratio is 0.75. The C/N ratios in the cases of g-$C_3N_4$ and *t*-$C_3N_4$ are found to be a similar result of theoretical value (0.66 and 0.69, respectively).

TEM analysis was carried out to characterize the structure of the as-prepared materials. The TEM images in Fig. 2d–f show that the tubular structure of *t*-$C_3N_4$ was well formed with diameters of ~ 50 nm when compared to the sheet-like morphology of g-$C_3N_4$. Moreover, $Fe_3O_4$ nanospheres with diameter of 2–5 nm were found to be dispersed on the surface of *t*-$C_3N_4$ (Fig. 2f). Moreover, EDS analysis was conducted and confirmed the existence of C, N, O, and Fe elements in $Fe_3O_4$/*t*-$C_3N_4$ (Fig. S3). Consequently, the well-dispersed $Fe_3O_4$ nanospheres on *t*-$C_3N_4$ will enhance electronic conductivity and provide additional LPS adsorption.

To evaluate the electronic conductivity of prepared materials, we assembled the cell (prepared materials coated cathode, separator, Li-metal anode, and electrolyte). In Fig. S4, the cell with $Fe_3O_4$/*t*-$C_3N_4$ material presents a smaller resistance ($R_{ct}$, see the electronic supplementary material for details) when compared to those of the as-prepared other cells. This was attributed to enhanced electronic conductivity from decorated $Fe_3O_4$ on *t*-$C_3N_4$, and the data suggest that $Fe_3O_4$/*t*-$C_3N_4$ can provide fast electronic transfer and enhance an efficient electrochemical system [4, 5, 8].

The morphological changes depending on the $Fe_3O_4$ loading amount are shown in Fig. S5. Using a low concentration of the Fe-based precursor, only a few $Fe_3O_4$ nanospheres were sparsely attached on the surface of *t*-$C_3N_4$, whereas the $Fe_3O_4$ nanospheres were aggregated on the surface of *t*-$C_3N_4$ when using a high concentration of the Fe precursor. According to Liao et al. and Ding et al., the binding energy between $C_3N_4$ and $Li_2S_6$ is 4.37 times higher than that between $Fe_3O_4$ and $Li_2S_6$ from density functional theory computational calculations [24, 25]. Therefore, a dense $Fe_3O_4$ nanosphere surface may limit the chemical interaction of *t*-$C_3N_4$ with the LPS. The deposition of optimum amount of $Fe_3O_4$ nanospheres may enhance the electronic conductivity of the *t*-$C_3N_4$ and attribute the boosting of LPS adsorption.

Figure 3a shows the adsorption capability toward LPS exhibited by the as-prepared materials evaluated by ultraviolet–visible (UV–Vis) spectroscopy using a 0.5 mmol $L^{-1}$ $Li_2S_6$ DOL–DME solution containing 10 mg of the as-prepared materials [4, 26]. An absorption region of 240–420 nm can be observed in the LPS solution. The two characteristic peaks centered at 280 and 340 nm can be ascribed to the $S_6^{2-}$ species. After adding the four different materials (CB, g-$C_3N_4$, *t*-$C_3N_4$, and $Fe_3O_4$/*t*-$C_3N_4$) into the $Li_2S_6$ solution, the color of the solution was noticeably changed after 1 h

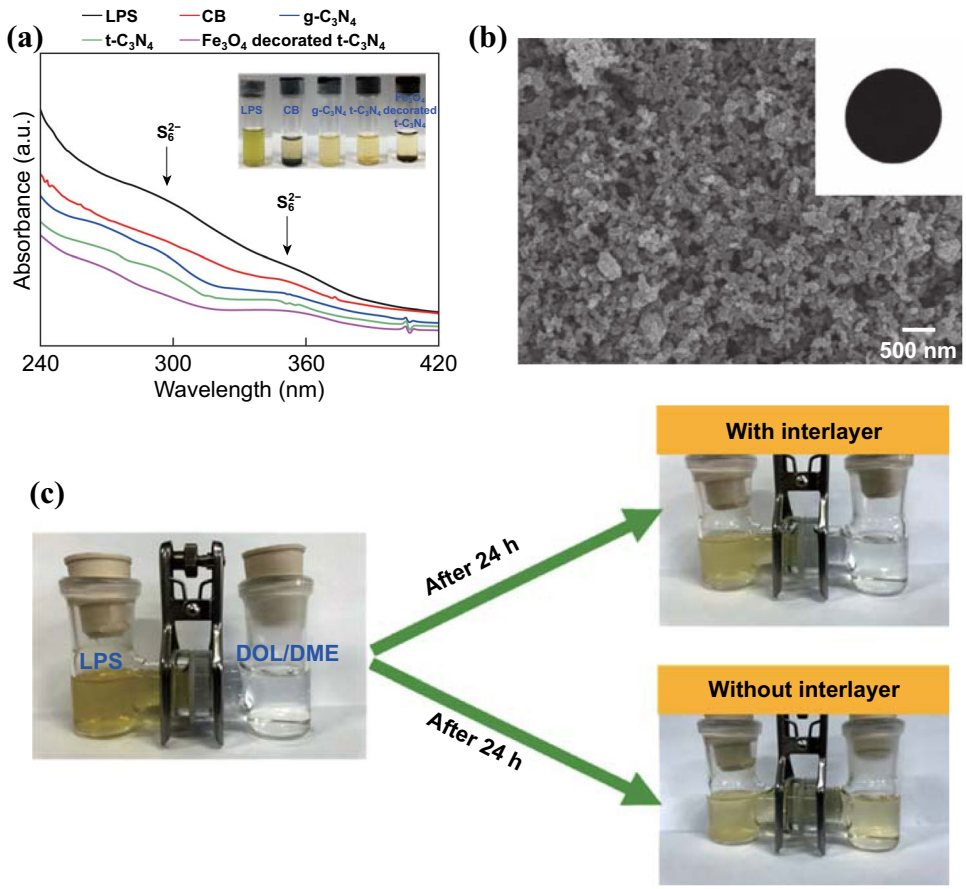


**Fig. 3** **a** UV–Vis spectra recorded for $Li_2S_6$, carbon black (CB), g-$C_3N_4$, *t*-$C_3N_4$, and $Fe_3O_4$/*t*-$C_3N_4$ as well as their corresponding optical images (inset). **b** SEM image of the surface of the interlayer constructed using the $Fe_3O_4$/*t*-$C_3N_4$. **c** Optical images obtained during the LPS adsorption test using an H-type cell with an $Fe_3O_4$/*t*-$C_3N_4$ interlayer and without interlayer

from dark yellow to light yellow (Fig. 3a (inset)). Moreover, the peak intensities of the $S_6^{2-}$ species decreased significantly after adding the materials with the greatest decrease in the absorbance observed at 280 and 340 nm displayed by the $Fe_3O_4$/*t*-$C_3N_4$ [4, 26]. These results clearly demonstrate that $Fe_3O_4$/*t*-$C_3N_4$ can efficiently adsorb the LPS due to its high surface area and high affinity toward LPS.

Figure S6 shows the $N_2$ adsorption isotherms obtained for g-$C_3N_4$, *t*-$C_3N_4$, and $Fe_3O_4$/*t*-$C_3N_4$. The Brunauer–Emmett–Teller (BET) specific surface area of the $Fe_3O_4$/*t*-$C_3N_4$ was estimated to be 71.27 $m^2\ g^{-1}$ from the adsorption isotherm, which was much higher than those of g-$C_3N_4$ (10.86 $m^2\ g^{-1}$) and *t*-$C_3N_4$ (33.71 $m^2\ g^{-1}$). The large surface area of $Fe_3O_4$/*t*-$C_3N_4$ will lead to effective LPS regulation, facile electronic transfer, and remarkable battery performance.

### 3.2 Fabrication of $Fe_3O_4$/*t*-$C_3N_4$ Interlayer and Evaluation of LPS Adsorption

An interlayer was prepared via a simple coating process using $Fe_3O_4$/*t*-$C_3N_4$, CB, and a polymer binder on a commercial Celgard separator. The surface morphology of the as-prepared interlayer was observed using SEM (Fig. 3b). Moreover, the cross-sectional morphology of the as-prepared interlayer is shown in Fig. S7. The thickness of the interlayer was controlled at ~ 10 μm; a thickness of ~ 10 μm is known to be appropriate without any significant disruption to ion transfer [27, 28].

Figure S8 shows that the interlayer based on $Fe_3O_4$/*t*-$C_3N_4$ presents stable mechanical properties upon folding. After five folding cycles, no damage was observed in the interlayer, such as cracks, tears, and exfoliation.


https://doi.org/10.1007/s40820-020-00475-5

In agreement with the results obtained during the LPS adsorption study (Fig. 3a), the interlayer prepared using the $Fe_3O_4$/*t*-$C_3N_4$ also exhibits the efficient regulation of LPS in the H-type cell test (Fig. 3c). After 24 h, H-type cell with interlayer did not allow the movement of LPS through passing the as-prepared interlayer, which means the efficient suppression of LPS. However, in the H-type cell without using interlayer, the left and right side of the H-type cell turned to similar color (light yellow), which means penetrating the LPS and reaching equilibrium state of LPS concentration. These results demonstrate that the application of $Fe_3O_4$/*t*-$C_3N_4$ as an interlayer for Li–S batteries can attribute to enhanced battery performance.

### 3.3 Electrochemical Characterization of Li–S Cell with $Fe_3O_4$/*t*-$C_3N_4$ Interlayer

Figure 4 shows the effects of the as-prepared interlayer on the battery performance investigated using electrochemical analysis. Figure 4a presents the galvanostatic charge–discharge curves obtained at 0.2 C after activating at 0.05 C for two cycles. The Li–S cell constructed using the $Fe_3O_4$/*t*-$C_3N_4$ interlayer exhibits an enhanced specific capacity of 1245 mAh $g^{-1}$, which indicates a 300 ~ 400% increase in capacity when compared to that of the Li–S cell constructed without an interlayer. Moreover, it shows a small voltage difference ($\Delta V_x$) between the charge and discharge plateaus (160 mV; Fig. 4b). A specific capacity of 901 mAh $g^{-1}$ and $\Delta V_x$ value of 250 mV was exhibited by the Li–S cell constructed using the g-$C_3N_4$ interlayer. The Li–S cell prepared using the *t*-$C_3N_4$ interlayer displays a specific capacity of 971 mAh $g^{-1}$ and $\Delta V_x$ value of 225 mV. The voltage difference observed between the charge and discharge plateaus shows the polarization and roundtrip energy efficiency of the cell. Lower polarization (lower voltage difference) represents a more kinetically efficient reaction process with a smaller barrier [29, 30]. These results are also consistent with the analysis through cyclic voltammograms in Fig. S9. Li–S cell with $Fe_3O_4$/*t*-$C_3N_4$ interlayer shows higher reduction peaks and a lower oxidation peak with large current density when compared to other two cells (with g-$C_3N_4$ interlayer and *t*-$C_3N_4$ interlayer). This suggests that the existence of the $Fe_3O_4$/*t*-$C_3N_4$ interlayer provides the efficient electrochemical redox process because of its increased electrical conductivity and strong adsorption for LPS [31, 32].

Figure 4c shows the electrochemical impedance spectroscopy (EIS) results obtained for the Li–S cells constructed using the various interlayers before cycling (see Figs. S10 and S11 for a detailed the EIS data and used EIS circuit). Before cycling, one depressed semicircle is observed, which

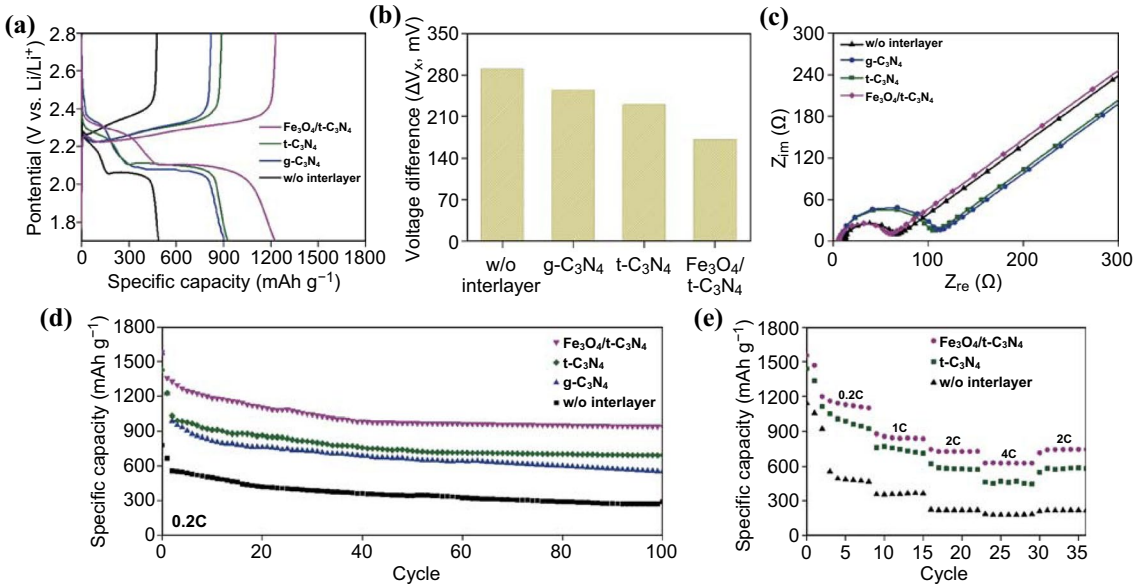


**Fig. 4** **a** Galvanostatic charge–discharge curves obtained for the as-prepared Li–S cells. **b** Voltage difference observed between the charge and discharge plateau obtained for the as-prepared Li–S cells. **c** EIS data obtained for the Li–S cells before cycling. **d** Discharging specific capacities of the Li–S cells observed at 0.2 C and **e** rate capability observed for the Li–S cells at 0.2, 1, 2, and 4 C

denotes the charge transfer resistance ($R_{ct}$) and characterizes the local redox reactions in which the active material obtains an electron from the conductive agent and captures a lithium ion from the liquid electrolyte [4, 25, 29]. Before cycling, the Li–S cells constructed with and without an interlayer using the $Fe_3O_4$/*t*-$C_3N_4$ exhibit lower $R_{ct}$ values when compared to the Li–S cells prepared using the g-$C_3N_4$, and *t*-$C_3N_4$. For the Li–S cells prepared with an interlayer consisting of g-$C_3N_4$, and *t*-$C_3N_4$, the diffusion of Li ions may be restricted by physical barrier effect. In addition, the resistance increases slightly resulted from their relatively low electronic conductivity. However, there was no increase in the resistance observed for the Li–S cell prepared using the $Fe_3O_4$/*t*-$C_3N_4$ interlayer due to the improved electronic conductivity provided by $Fe_3O_4$ [33].

Figure 4d shows the results obtained for the battery performance tests performed using the as-prepared interlayers (g-$C_3N_4$, *t*-$C_3N_4$, and $Fe_3O_4$/*t*-$C_3N_4$) as well as a comparison of their performance with the Li–S battery prepared without an interlayer. The Li–S cell without using interlayer showed an initial specific capacity of 540 mAh $g^{-1}$ at 0.2 C and a specific capacity of 262 mAh $g^{-1}$ after 100 cycles. The Li–S cells prepared using an g-$C_3N_4$ and *t*-$C_3N_4$ interlayer exhibit further improved battery performance when compared to the Li–S cells constructed with and without an interlayer (for the g-$C_3N_4$ interlayer, the specific capacity was 603 mAh $g^{-1}$ at 0.2 C after 100 cycles; the *t*-$C_3N_4$ interlayer shows a specific capacity of 810 mAh $g^{-1}$ at 0.2 C after 100 cycles). As expected, g-$C_3N_4$ and *t*-$C_3N_4$ enhance the LPS adsorption capacity, which can improve the battery performance. Moreover, the Li–S cell prepared using the $Fe_3O_4$/*t*-$C_3N_4$ interlayer delivers a remarkable enhancement, such as an initial discharge capacity of 1255 mAh $g^{-1}$ at 0.2 C and a retained discharging capacity of 1048 mAh $g^{-1}$ after 100 cycles. In comparison with the controlled amount of $Fe_3O_4$/*t*-$C_3N_4$ interlayer (Fig. S12), the Li–S cell constructed using the $Fe_3O_4$/*t*-$C_3N_4$ interlayer shows a 400% improved battery performance compared with Li–S cell without using interlayer. Figure S10 shows the EIS analysis results obtained after 100 cycles. The Li–S cell prepared with the $Fe_3O_4$/*t*-$C_3N_4$ interlayer presents a smaller resistance ($R_{int}$ and $R_{ct}$, see the electronic supplementary material for details) when compared to those of the as-prepared Li–S cell. This was attributed to the activation of the sulfur cathode during cycling, and the data suggest that $Fe_3O_4$/*t*-$C_3N_4$ facilitates relatively fast electronic transfer and provides an efficient electrochemical system for suppressing the LPS shuttle effect, which leads to its high battery performance. Moreover, after cycling, the surface of interlayer did not present crack and collapse of interlayer materials (Fig. S13).

The fabricated Li–S cells were evaluated in terms of their rate capabilities with current densities ranging from 0.05 to 4 C to further analyze the battery performance, as shown in Fig. 4e. The average discharge capacities obtained for the Li–S cell constructed using a $Fe_3O_4$/*t*-$C_3N_4$ interlayer show highly stable rate capabilities comparable to those demonstrated by the Li–S cells prepared with and without an interlayer prepared using *t*-$C_3N_4$. Moreover, the Li–S cell constructed using a $Fe_3O_4$/*t*-$C_3N_4$ interlayer delivers a desirable battery performance at a high C-rate (830 mAh $g^{-1}$ at 2 C and 680 mAh $g^{-1}$ at 4 C). The high regulation of the LPS and enhanced electronic conductivity of the as-prepared interlayer result in a high performance of the Li–S battery at a high C-rate.

For commercial applications, the loading density of sulfur and the C-rate are important factors [4, 30]. Figure 5a

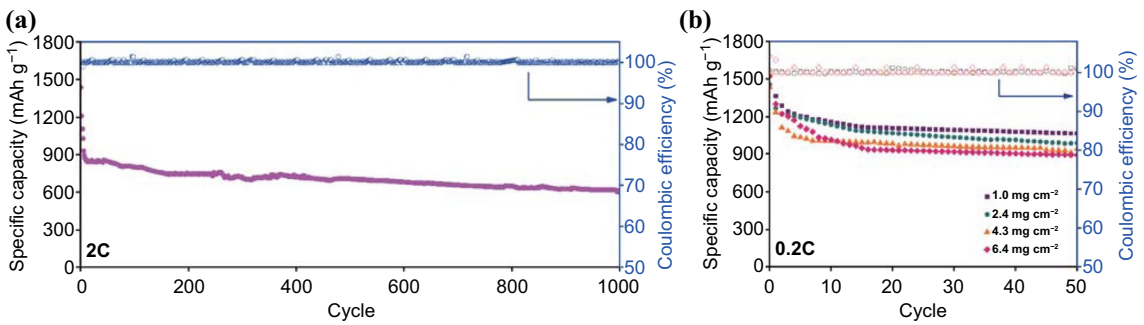


**Fig. 5** **a** Discharge specific capacities obtained for the Li–S cell prepared with an $Fe_3O_4$-decorated *t*-$C_3N_4$ interlayer operated at 2 C during the stability test and **b** discharge specific capacity of the high-sulfur-loading cathode $Fe_3O_4$/*t*-$C_3N_4$ interlayer operated at 0.2 C

 https://doi.org/10.1007/s40820-020-00475-5

shows the results of the long-term cycling test obtained for the Li–S cell prepared with the $Fe_3O_4$/*t*-$C_3N_4$ interlayer operated at 2 C. The Li–S cell with the $Fe_3O_4$/*t*-$C_3N_4$ interlayer exhibited an initial discharge capacity of 828 mAh $g^{-1}$ at 2 C, at which most portable batteries are rated, and its capacity remained at 658 mAh $g^{-1}$ over 1000 cycles (a capacity retention decay of 0.02% per cycle). The long-term cycling test results demonstrate the remarkable effects of regulating the LPS and the enhanced electronic properties of the $Fe_3O_4$/*t*-$C_3N_4$ interlayer.

Furthermore, an increased sulfur loading is important for the commercial application of LSBs. For example, the batteries used in electric vehicles (EVs) require a sulfur loading of > 2.0 mg $cm^{-2}$ for a specific energy density of > 400 Wh $kg^{-1}$ [4, 34]. Thus, the specific capacity of the Li–S cell prepared with the $Fe_3O_4$/*t*-$C_3N_4$ interlayer was evaluated as a function of the sulfur loading (1.0, 2.4, 4.3, and 6.4 mg $cm^{-2}$) at 0.2 C. Figure 5b shows that the Li–S cell maintained its stability upon increasing the sulfur loading and its Coulombic efficiency reached ~ 99%. The efficiently regulated LPS and enhanced electronic properties of $Fe_3O_4$/*t*-$C_3N_4$ result in long-term cycling stability even with a high-sulfur loading.

Table S3 shows a comparison of the battery performance observed for the Li–S cells prepared using various N-doped carbonaceous-based interlayers. Among the interlayers studied, the $Fe_3O_4$/*t*-$C_3N_4$ interlayer induces the highest cycling stability with a capacity decay of 0.02% per cycle at a high C-rate (2 C). Therefore, based on these results, employing a $Fe_3O_4$/*t*-$C_3N_4$ interlayer in an LSB will facilitate efficient battery usage and result in impressive battery performance.

## 4 Conclusions

We have explored the hierarchical $Fe_3O_4$/*t*-$C_3N_4$ nanostructures as an interlayer for advanced LSBs. *t*-$C_3N_4$ has a high affinity toward LPS and increased surface area, and the embedded $Fe_3O_4$ nanospheres on the surface of *t*-$C_3N_4$ enhance the electrical conductivity and LPS anchoring properties. The synergistic effect between the *t*-$C_3N_4$ and embedded $Fe_3O_4$ nanospheres exhibits a remarkable battery performance with a low capacity decay per cycle of 0.02% at 2 C over 1000 cycles as well as stable cycling at 6.4 mg $cm^{-2}$ for a high-sulfur-loading cathode. The $Fe_3O_4$/*t*-$C_3N_4$ interlayer can be employed in various energy storage devices as well as advanced LSBs.

**Acknowledgements** This work was supported by the Basic Science Research Program through the National Research Foundation of Korea (NRF) funded by the Ministry of Science and ICT (NRF-2019R1A2C1003594 and NRF-2019R1A2C1003551).



**Electronic supplementary material** The online version of this article (https://doi.org/10.1007/s40820-020-00475-5) contains supplementary material, which is available to authorized users.

## References

1. L. Hencz, H. Chen, H.Y. Ling, Y. Wang, C. Lai, H. Zhao, S. Zhang, Housing sulfur in polymer composite frameworks for Li–S batteries. Nano-Micro Lett. **11**, 17 (2019). https://doi.org/10.1007/s40820-019-0249-1
2. C. Wang, X. Wang, Y. Wang, J. Chen, H. Zhou, Y. Huang, Macroporous free-standing nano-sulfur/reduced graphene oxide paper as stable cathode for lithium-sulfur battery. Nano Energy **11**, 678–686 (2015). https://doi.org/10.1016/j.nanoen.2014.11.060
3. Y. Ansari, S. Zhang, B. Wen, F. Fan, Y.-M. Chiang, Stabilizing Li–S battery through multilayer encapsulation of sulfur. Adv. Energy Mater. **9**(1), 1802213 (2019). https://doi.org/10.1002/aenm.201802213
4. S. Kim, M. Cho, Y. Lee, Multifunctional chitosan–RGO network binder for enhancing the cycle stability of Li–S batteries. Adv. Funct. Mater. **30**(10), 1907680 (2020). https://doi.org/10.1002/adfm.201907680
5. Y. Fan, Z. Yang, W. Hua, D. Liu, T. Tao et al., Functionalized boron nitride nanosheets/graphene interlayer for fast and long-life lithium–sulfur batteries. Adv. Energy Mater. **7**(13), 1602380 (2017). https://doi.org/10.1002/aenm.201602380
6. S. Lin, M.K. Shafique, Z. Cai, J. Xiao, Y. Chen, Y. Wang, X. Hu, Three-dimensional-ordered porous nanostructures for lithium–sulfur battery anodes and cathodes confer superior energy storage performance. ACS Nano **13**(11), 13037–13046 (2019). https://doi.org/10.1021/acsnano.9b05718

7. Y.-S. Su, A. Manthiram, Lithium–sulphur batteries with a microporous carbon paper as a bifunctional interlayer. Nat. Commun. **3**(1), 1166 (2012). https://doi.org/10.1038/ncomms2163
8. J.-Y. Hwang, H.M. Kim, S.-K. Lee, J.-H. Lee, A. Abouimrane et al., High-energy, high-rate, lithium–sulfur batteries: synergetic effect of hollow $TiO_2$-webbed carbon nanotubes and a dual functional carbon-paper interlayer. Adv. Energy Mater. **6**(1), 1501480 (2016). https://doi.org/10.1002/aenm.201501480
9. P. Cheng, P. Guo, D. Liu, Y. Wang, K. Sun, Y. Zhao, D. He, $Fe_3O_4$/RGO modified separators to suppress the shuttle effect for advanced lithium-sulfur batteries. J. Alloys Compd. **784**, 149–156 (2019). https://doi.org/10.1016/j.jallcom.2019.01.041
10. N. Zheng, G. Jiang, X. Chen, J. Mao, N. Jiang, Y. Li, Battery separators functionalized with edge-rich $MoS_2$/C hollow microspheres for the uniform deposition of $Li_2S$ in high-performance lithium–sulfur batteries. Nano-Micro Lett. **11**(1), 43 (2019). https://doi.org/10.1007/s40820-019-0275-z
11. X. Zuo, M. Zhen, C. Wang, Ni@n-doped graphene nanosheets and CNTs hybrids modified separator as efficient polysulfide barrier for high-performance lithium sulfur batteries. Nano Res. **12**(4), 829–836 (2019). https://doi.org/10.1007/s12274-019-2298-7
12. X. Liang, C.Y. Kwok, F. Lodi-Marzano, Q. Pang, M. Cuisinier et al., Tuning transition metal oxide–sulfur interactions for long life lithium sulfur batteries: the "goldilocks" principle. Adv. Energy Mater. **6**(6), 1501636 (2016). https://doi.org/10.1002/aenm.201501636
13. Z. Cao, J. Zhang, Y. Ding, Y. Li, M. Shi et al., In situ synthesis of flexible elastic n-doped carbon foam as a carbon current collector and interlayer for high-performance lithium sulfur batteries. J. Mater. Chem. A **4**(22), 8636–8644 (2016). https://doi.org/10.1039/C6TA01855F
14. H. Wu, Y. Huang, S. Xu, W. Zhang, K. Wang, M. Zong, Fabricating three-dimensional hierarchical porous n-doped graphene by a tunable assembly method for interlayer assisted lithium-sulfur batteries. Chem. Eng. J. **327**, 855–867 (2017). https://doi.org/10.1016/j.cej.2017.06.164
15. V. Do, M.S. Deepika, M.S. Kim, K.R. Kim, W.I.Cho Lee, Carbon nitride phosphorus as an effective lithium polysulfide adsorbent for lithium–sulfur batteries. ACS Appl. Mater. Interfaces **11**(12), 11431–11441 (2019). https://doi.org/10.1021/acsami.8b22249
16. Z. Meng, Y. Xie, T. Cai, Z. Sun, K. Jiang, W.-Q. Han, Graphene-like g-$C_3N_4$ nanosheets/sulfur as cathode for lithium–sulfur battery. Electrochim. Acta **210**, 829–836 (2016). https://doi.org/10.1016/j.electacta.2016.06.032
17. A. Wang, C. Wang, L. Fu, W. Wong-Ng, Y. Lan, Recent advances of graphitic carbon nitride-based structures and applications in catalyst, sensing, imaging, and LEDs. Nano-Micro Lett. **9**(4), 47 (2017). https://doi.org/10.1007/s40820-017-0148-2
18. J. He, L. Luo, Y. Chen, A. Manthiram, Yolk–shelled C@$Fe_3O_4$ nanoboxes as efficient sulfur hosts for high-performance lithium–sulfur batteries. Adv. Mater. **29**(34), 1702707 (2017). https://doi.org/10.1002/adma.201702707
19. Z. Jin, Q. Zhang, S. Yuan, T. Ohno, Synthesis high specific surface area nanotube g-$C_3N_4$ with two-step condensation treatment of melamine to enhance photocatalysis properties. RSC Adv. **5**(6), 4026–4029 (2015). https://doi.org/10.1039/C4RA13355B
20. G. Dong, Y. Zhang, Q. Pan, J. Qiu, A fantastic graphitic carbon nitride (g-$C_3N_4$) material: electronic structure, photocatalytic and photoelectronic properties. J. Photochem. Photobiol. C **20**, 33–50 (2014). https://doi.org/10.1016/j.jphotochemrev.2014.04.002
21. C.G. Liu, X.T. Wu, X.F. Li, X.G. Zhang, Synthesis of graphene-like g-$C_3N_4$/$Fe_3O_4$ nanocomposites with high photocatalytic activity and applications in drug delivery. RSC Adv. **4**(107), 62492–62498 (2014). https://doi.org/10.1039/C4RA10616D
22. M.J. Lima, M.J. Sampaio, C.G. Silva, A.M.T. Silva, J.L. Faria, Magnetically recoverable $Fe_3O_4$/g-$C_3N_4$ composite for photocatalytic production of benzaldehyde under UV-led radiation. Catal. Today **328**, 293–299 (2019). https://doi.org/10.1016/j.cattod.2018.11.018
23. P. Sharma, Y. Sasson, A photoactive catalyst Ru–g-$C_3N_4$ for hydrogen transfer reaction of aldehydes and ketones. Green Chem. **19**(3), 844–852 (2017). https://doi.org/10.1039/C6GC02949C
24. K. Liao, P. Mao, N. Li, M. Han, J. Yi, P. He, Y. Sun, H. Zhou, Stabilization of polysulfides via lithium bonds for Li–S batteries. J. Mater. Chem. A **4**(15), 5406–5409 (2016). https://doi.org/10.1039/C6TA00054A
25. M. Ding, S. Huang, Y. Wang, J. Hu, M.E. Pam et al., Promoting polysulfide conversion by catalytic ternary $Fe_3O_4$/carbon/graphene composites with ordered microchannels for ultra-high-rate lithium–sulfur batteries. J. Mater. Chem. A **7**(43), 25078–25087 (2019). https://doi.org/10.1039/C9TA06489C
26. S. Kim, M. Cho, C. Chanthad, Y. Lee, New redox-mediating polymer binder for enhancing performance of Li–S batteries. J. Energy Chem. **44**, 154–161 (2020). https://doi.org/10.1016/j.jechem.2019.09.001
27. R. Singhal, S.-H. Chung, A. Manthiram, V. Kalra, A free-standing carbon nanofiber interlayer for high-performance lithium–sulfur batteries. J. Mater. Chem. A **3**(8), 4530–4538 (2015). https://doi.org/10.1039/C4TA06511E
28. L. Yang, G. Li, X. Jiang, T. Zhang, H. Lin, J.Y. Lee, Balancing the chemisorption and charge transport properties of the interlayer in lithium–sulfur batteries. J. Mater. Chem. A **5**(24), 12506–12512 (2017). https://doi.org/10.1039/C7TA01352C
29. J. Yan, X. Liu, B. Li, Capacity fade analysis of sulfur cathodes in lithium–sulfur batteries. Adv. Sci. **3**(12), 1600101 (2016). https://doi.org/10.1002/advs.201600101
30. S. Kim, M. Cho, Y. Lee, High-performance Li–Se battery enabled via a one-piece cathode design. Adv. Energy Mater. **10**(5), 1903477 (2020). https://doi.org/10.1002/aenm.201903477
31. Y. Guo, J. Li, R. Pitcheri, J. Zhu, P. Wen, Y. Qiu, Electrospun $Ti_4O_7$/C conductive nanofibers as interlayer for lithium-sulfur batteries with ultra long cycle life and high-rate capability.


 https://doi.org/10.1007/s40820-020-00475-5

Chem. Eng. J. **355**, 390–398 (2019). https://doi.org/10.1016/j.cej.2018.08.143

32. Q. Pang, D. Kundu, M. Cuisinier, L.F. Nazar, Surface-enhanced redox chemistry of polysulphides on a metallic and polar host for lithium-sulphur batteries. Nat. Commun. **5**(1), 4759 (2014). https://doi.org/10.1038/ncomms5759
33. V. Sivakumar, S. Kumar, C. Ross, Y. Shao-Horn, Electrochemical lithium insertion of iron oxide spinel thin films and nanoparticles: changes in structure and magnetic properties. ECS Trans. **2**(8), 1–11 (2007). https://doi.org/10.1149/1.2424283
34. M.A. Pope, I.A. Aksay, Structural design of cathodes for Li–S batteries. Adv. Energy Mater. **5**(16), 1500124 (2015). https://doi.org/10.1002/aenm.201500124